



Fabrication and characterization of SiC whiskers toughened Al₂O₃ paste for stereolithography 3D printing applications

Hongyu Xing^{a, b, c}, Bin Zou^{a, b, c, *}, Xinfeng Wang^{a, b, c}, Yifan Hu^{a, b, c},
Chuanzhen Huang^{a, b, c}, Kai Xue^{a, b, c}

^a Centre for Advanced Jet Engineering Technologies (CaJET), School of Mechanical Engineering, Shandong University, Jinan, 250061, PR China

^b Key Laboratory of High Efficiency and Clean Mechanical Manufacture, Shandong University, Ministry of Education, PR China

^c National Demonstration Center for Experimental Mechanical Engineering Education, Shandong University, PR China



ARTICLE INFO

Article history:

Received 8 January 2020
Received in revised form
9 February 2020
Accepted 12 February 2020
Available online 14 February 2020

Keywords:

Stereolithography
3D printing
SiC_w/Al₂O₃ paste
Fracture toughness
Rheological properties

ABSTRACT

To prevent the agglomeration of silicon carbide whiskers (SiC_w) in photosensitive ceramic paste, a butanone-ethanol azeotropic solvent is employed to facilitate the dispersion of alumina particles, SiC whiskers and UV resins. Moreover, SiC_w/Al₂O₃ ceramic pastes, with 5–15 vol % SiC_w, are prepared by using ball milling, stirring and distillation processes. The mixture of butanone-ethanol solvent and resins can be effectively separated at 70 °C without weakening the polymerization of UV resin. Moreover, an empirical equation is established to evaluate the relationship between SiC_w content, aspect ratio and viscosity of resulting ceramic paste. The 15 vol % SiC_w/Al₂O₃ composite ceramic, with SiC_w aspect ratio of 50, renders higher resistance to liquid flow and results in a high viscosity of 30,000 mPa s at the shear rate of 30 s⁻¹. Furthermore, a modified equation is established to predicate the curing depth of ceramic pastes with different amounts of SiC_w, where 15 vol % SiC_w/Al₂O₃ composite results in higher light scattering properties, leading to lowest C_d of ~0.061 mm. Finally, the complex-shaped SiC_w/Al₂O₃ ceramic component, prepared by SL 3D printing technology, debinding and sintering processes, exhibited a superior fracture toughness of 7.1 ± 1.20 MPa m^{1/2} and a higher hardness of 17.6 ± 0.78 GPa.

© 2020 Elsevier B.V. All rights reserved.

1. Introduction

α-Al₂O₃ belongs to the trigonal system and is widely employed in aerospace, mechanical processing, electronic communications and medical devices due to its unique advantages, such as low chemical activity, high-temperature stability, excellent electrical and mechanical properties [1]. However, pure alumina ceramics cannot meet the requirements of functional and structural complexities in some special working conditions due to single-phase composition and brittleness, as evidenced by the low fracture toughness of 3 MPa m^{1/2} [2]. Therefore, a reinforcement phase is added into the Al₂O₃ matrix to fabricate complex-shaped ceramic parts, which expands the application's horizon of alumina-based composites. One should note that the addition of a secondary phase can improve the toughness, thermal shock resistance and fatigue strength of Al₂O₃ ceramics. For instance, Xue et al. [3] have

prepared Al₂O₃ cores for high-temperature hollow blades by adding graphite and oleic acid. The as-prepared alumina cores exhibited a porosity of 47.8% and corroded in boiling alkaline solution after 1.5 h, which significantly improved the stripping efficiency. Liao et al. [4] have fabricated Al₂O₃ transparent glass by doping Fe and Cr particles. At the doping content of 0.5 wt %, the transparent ceramic surface rendered obvious magnetism with the specific magnetization of 0.12 emu/g. Liu et al. [5] have synthesized Al₂O₃ composite ceramic tools by adding SiC particles and whiskers, resulting in flexural strength, fracture toughness and hardness reached of 715 MPa, 8.2 MPa m^{1/2} and 22.57 GPa, respectively. By adding Ni and Mo metallic particles, Wang et al. [6] have prepared cermet tools for the development and application of micro-milling cutters. In terms of morphology, the additives are often granular, short whiskers and long fibrous. However, the dispersion of whiskers and fibers in a ceramic matrix is a challenging task [7].

The three-dimensional (3D) printing of ceramics can be carried out by using selective laser sintering (SLS), fusing deposit ceramics (FDC), direct 3D printing (3DP), inkjet printing (IJP) and stereo light curing (SL) [8–12]. The raw materials for 3D printing can be divided

* Corresponding author. Shandong University, 17923 Jing Shi Road, Jinan, 250061, PR China.

E-mail address: zb78@sdu.edu.cn (B. Zou).

into four categories, including thin sheets, wires, powder and slurry [13]. For instance, Griffin et al. [14] have fabricated ZrO_2/Al_2O_3 composites by using thin sheets of ceramic particles and laminated object manufacturing (LOM) technology. Bandyopadhyay et al. [15] have utilized ceramic particles and polypropylene thermoplastic binder to fabricate filamentous raw materials and, then, prepared $Al_2O_3-SiO_2-Al$ ceramic/metal composites by using FDC technology. However, they have obtained low surface resolution due to the lower printing accuracy and obvious step effects. Shahzad and Yoo [16,17] have prepared complex-shaped Al_2O_3 parts by using SLS and 3DP technologies, resulting in a sintered density of 88% and 99.2%, respectively. However, the bending strength of SLS and 3DP-fabricated parts did not exceed 330 MPa, which needs to be further improved. In addition, Larson et al. [18] have prepared SiC ceramic parts by using 5–15 vol % ceramic ink via IJP, which resulted in a low bending strength of only 70.4 MPa and a relative density of 48.9%. Griffith et al. [19–22] have prepared Al_2O_3 composites from the photosensitive slurry, with a solid content of >40 vol %, via SL technology and attained a relative density of ~100% after debinding and sintering. One should note that the SL 3D printing technology renders unique advantages, such as high accuracy, excellent mechanical properties and superior density. Furthermore, the utilization of ceramic pastes, with a higher amount of solid content, can avoid the addition of support during 3D printing and reduce the shrinkage of green body during sintering, ensuring the surface quality and dimensional accuracy of ceramics [23]. However, the high viscosity of ceramic pastes sharply increases with the increase of solid content, which hinders the uniform dispersion of secondary additives, such as whiskers and fibers. Moreover, the whiskers with a certain aspect ratio consume more energy and render more resistance to fluids than spherical particles, further hindering the dispersion of whiskers in the ceramic matrix [24]. Furthermore, the agglomeration of whiskers hinders the densification during sintering [25].

Therefore, a novel technology is proposed to prepare a photosensitive paste, i.e., SiC-toughened Al_2O_3 (SiC_w/Al_2O_3) composite, which can prevent the agglomeration of whiskers. First, the whiskers are dispersed in the azeotropic solvent by using an FEG-400 surface modifier and subsequent drying at 70 °C. Then, the low boiling point impregnant system is utilized to facilitate mixing and dispersing of particles, whiskers and photosensitive organic compounds. Then, SiC_w/Al_2O_3 ceramic pastes, consisting of total solid content of 50 vol % and whiskers content of 5–15 vol %, are prepared by using ball milling, stirring and distillation process. Simultaneously, the influence of different solvents on the photopolymerization of photosensitive organic compounds and dispersion of whiskers in the ceramic paste is systematically analyzed. Moreover, the effect of SiC_w content on rheological and curing properties of ceramic pastes is studied in detail. Finally, complex-shaped SiC_w/Al_2O_3 ceramic parts are fabricated by using SL 3D printing. The surface quality, mechanical properties and microstructure of SiC_w/Al_2O_3 ceramic parts are studied.

2. Experimental procedure

2.1. Preparation of UV-curable SiC_w/Al_2O_3 ceramic paste

Briefly, 70 wt% ditrimethylolpropane tetraacrylate (Di-TMPTA, DSM-AGI Holland) and 30 wt% hexamethylene diacrylate (HDDA, Sigma Aldrich, USA) were used as UV resins. The polymerization was carried out by using a 1-Hydroxycyclohexyl phenyl ketone photoinitiator (Irgacure 184, BASF, Germany). The $\alpha-Al_2O_3$ particles (refractive index: 1.52), with the mean particle size (d_{50}) of 1 μm , and SiC_w whiskers (refractive index: 2.65), with a diameter of

0.5 μm and length/diameter ratio of 10–70, were used as the matrix and secondary materials, as shown in Fig. 1(a, b). Moreover, polyethylene glycol (PEG-400, Energy Chemicals, China) and stearic acid (SA, Energy Chemicals, China) were used to improve the dispersion uniformity of SiC_w whiskers and Al_2O_3 particles. In addition, ethanol, acetone, butanone, butanone-ethanol azeotrope were used as low-boiling point impregnant systems to dissolve UV resins and mixed powders.

The preparation of SiC_w/Al_2O_3 ceramic paste is illustrated in Fig. (2a–c). First, 2.5 wt % dilute solution was prepared by mixing PEG-400 surfactant (1.5 wt% of the whiskers) in ethanol. The SiC_w whiskers were dispersed in PEG-400 dilute solution by using ultrasonic vibrations for 2 h and subsequent drying, as shown in Fig. 1c. Then, the dispersed whiskers and Al_2O_3 powders were ball-milled for 12 h with SA dispersant (1.2 wt % of Al_2O_3 particles) to obtain SiC_w/Al_2O_3 mixture. The volume content of SiC_w was 5%, 10% and 15%, respectively. Second, the UV-resin was prepared by using Di-TMPTA, HDDA monomer and 4 wt% (with respect to the mass of resin) photoinitiator 184 at 40 °C under ultrasonic vibrations for 0.5 h. However, the whiskers have been partially agglomerated after the direct mixing of SiC_w/Al_2O_3 powder with resin, as shown in Fig. 1 (d). The dispersion of whiskers is hindered by the larger flow resistance of whiskers than spherical particles. Hence, each low-boiling point solvents was mixed with pre-mixed resin in a volume ratio of 1/2. Then, the as-prepared SiC_w/Al_2O_3 powder was added to the pre-mixture with resin and organic solvent, followed by high-speed stirring for 12 h. Finally, 50 vol % SiC_w/Al_2O_3 paste was obtained by evaporating the dispersed solvents during subsequent low-speed stirring, as shown in Fig. 2 (b).

2.2. Preparation of complex-shaped SiC_w/Al_2O_3 ceramic components

To demonstrate the potential of SL technology, the CAD model was imported into the Ceramaker300 system (3D CERAM, France), as illustrated in Fig. 3a–c. Then, an ultraviolet laser, with a wavelength of 355 nm, was scanned over the ceramics paste to create SiC_w/Al_2O_3 ceramic green body in a layer-by-layer fashion (Fig. 3d). Then, SiC_w/Al_2O_3 ceramic was prepared via debinding and sintering processes. Briefly, the green body was heated to 700 °C at 0.2 °C/min and held for 2 h under argon atmosphere to remove the binder (RS 80/300/11, Nabertherm, Germany). Then, the samples were heated to 1750 °C at the heating rate of 5 °C/min and held for 0.5 h with argon atmosphere (FPW12-5SP, FCT, Germany), resulting in SiC_w/Al_2O_3 ceramics with honeycomb structure (Fig. 3e). The dimensions of 3D printed green body and sintered parts were measured by microscopy and compared CAD model. The results revealed that the diameter of the green body was 99.95 mm and the thickness of honeycomb wall was 0.777 mm, which are 0.05 mm and 0.023 mm lower than the corresponding designed dimensions. Therefore, the size accuracy of SL 3D printing of as-prepared SiC_w/Al_2O_3 paste was found to be ~0.025 mm. After sintering, the diameter and wall thickness were found to be 84.359 mm and 0.663 mm, corresponding to a shrinkage rate of 15.6% and 14.7%, respectively.

2.3. Characterization

Fourier transform infrared (FTIR) spectra of UV-cured resins were obtained by using an FTIR spectrometer (VERTEX-70, Bruker, Germany). Rheological properties of UV-curable pastes were assessed by using a rotational rheometer (MCR302, Anton paar, Austria) under different shear rates, ranging from 1 to 100 s^{-1} . The microstructure of whiskers dispersion and sintered SiC_w/Al_2O_3 parts were investigated by using SEM (SUPRA55, ZEISS, German),

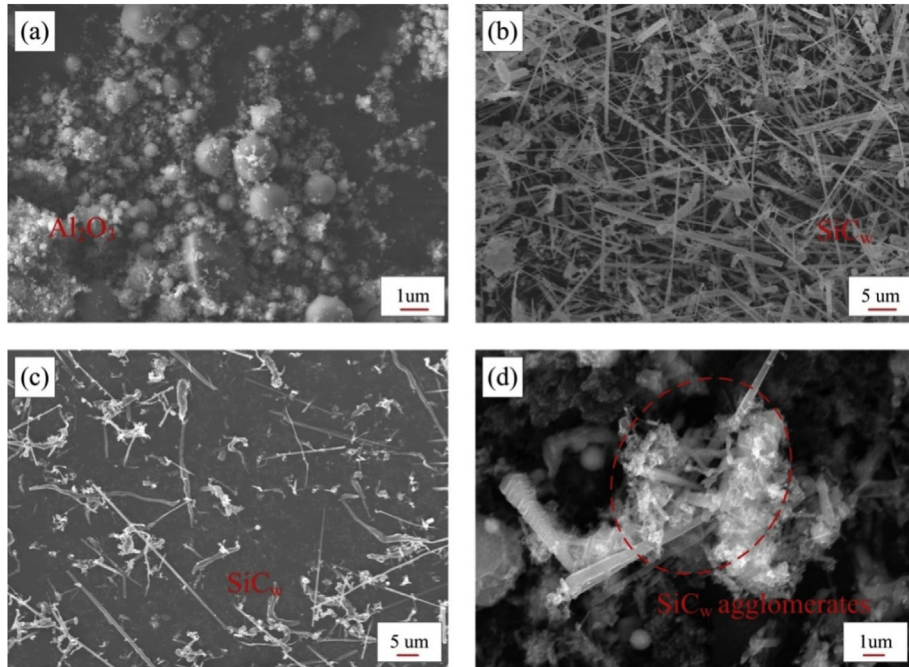


Fig. 1. SEM images of paste mixtures: (a) as-received Al_2O_3 , (b) as-received SiC whiskers, (c) dispersed SiC whiskers, (d) agglomerates SiC_w after direct mixing of powder in the resin matrix.

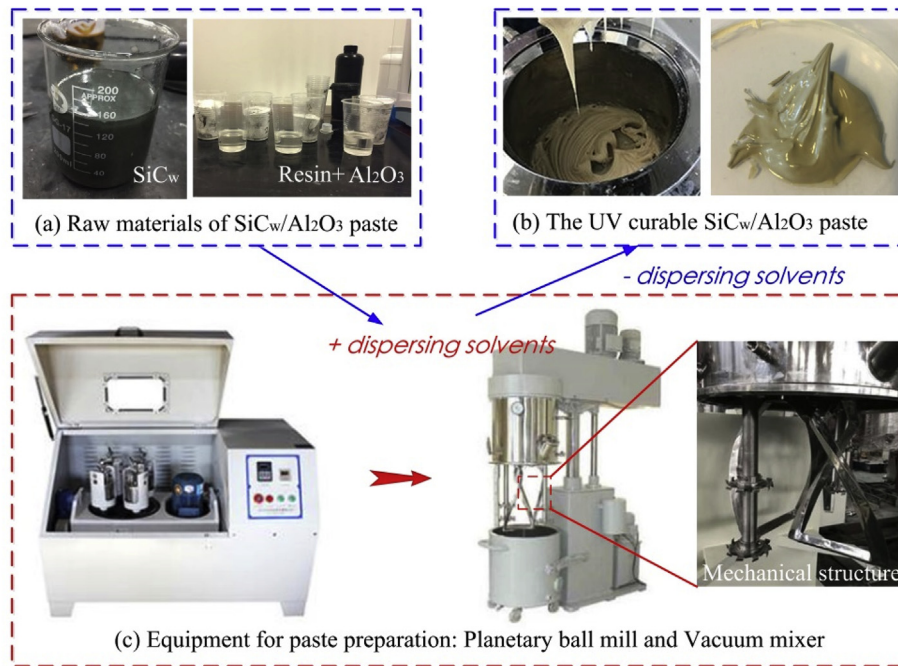


Fig. 2. Schematic illustration of SiC_w/Al₂O₃ paste preparation for SL-3D printing.

equipped with an energy-dispersive spectrometer (EDS, PV9900, Philips, Netherlands) for compositional analysis. Meanwhile, the SiC_w/Al₂O₃ bars were manufactured by using the SL 3D printing and sintering process to evaluate the mechanical properties of manufactured SiC_w/Al₂O₃ components. An LSM microscope (VK-X200K, KEYENCE, Japan) was utilized to assess the surface roughness and morphology.

3. Results and discussion

3.1. Effect of organic solvents on SiC_w/Al₂O₃ photosensitive paste

3.1.1. Separation and polymerization ability of solvent-resin mixtures

Different dispersion solvents were selected to reduce the viscosity of the mixture of SiC_w, Al₂O₃ particles and photosensitive

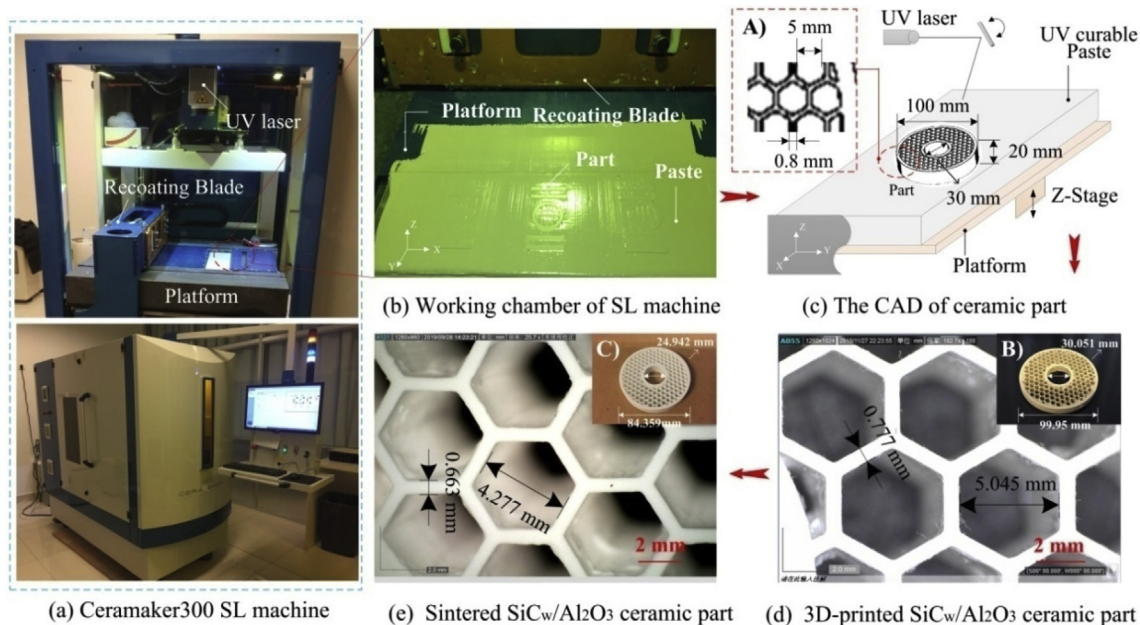


Fig. 3. Schematic illustration of complex-shaped $\text{SiC}_w/\text{Al}_2\text{O}_3$ component fabrication via SL 3D technology.

resin. The given experiment was carried out to analyze the separability of solvents and UV resins. 10 g of each solvent was mixed with 20 g of Di-TMPTA-based photosensitive resin. Then, the solvent-resin mixtures were evaporated at 70°C in vacuum and weighed every 0.5 h. Fig. 4 shows that the acetone-resin mixture exhibited rapid weight loss during the initial 1 h, whereas the ethanol-resin mixture rendered minimum weight loss, which is highly undesirable for separation efficiency. During 60–120 min, the weight loss rate of acetone-resin mixture slowed down but remained faster than other three solvent-resin mixtures. After 120 min, the weight of each mixture attained a stable state (~ 20 g), indicating that the solvents (acetone, butanone and butanone-ethanol azeotrope) are separated from the resins.

The following experiment was carried out to analyze the influence of solvent addition and evaporation on the photopolymerization of resins. First, the mixtures were evaporated for

2 h and UV-cured under ultraviolet light of 350 mW. Then, the thickness and infrared spectra of UV-cured samples were measured and compared with pure Di-TMPTA-based resin. As shown in Fig. 4A, the curing depth (C_d) of ethanol-resin, acetone-resin, butanone-resin and butanone-ethanol azeotrope-resin was 0.4 mm, 0.37 mm, 0.39 mm and 0.4 mm, respectively. Hence, the acetone-resin group rendered the smallest curing depth. Moreover, the warpage deformation of acetone-treated resin was significantly higher than other three groups. It can be inferred that the excessive volatilization rate of acetone rendered a negative influence on curing thickness and accuracy of as-prepared resins. Furthermore, the cured were analyzed by using FTIR spectra, as shown in Fig. 5 (a). The absorption peaks at 1724 cm^{-1} and 1188 cm^{-1} correspond to stretching vibrations of ester carboxyl ($-\text{COOR}$) and ether group ($\text{C}-\text{O}-\text{C}$) of the photosensitive resin, respectively. Also, the stretching vibration peak of unsaturated double bond ($\text{C}=\text{C}$), originating from acrylic resin, was found at 1637 cm^{-1} , where the

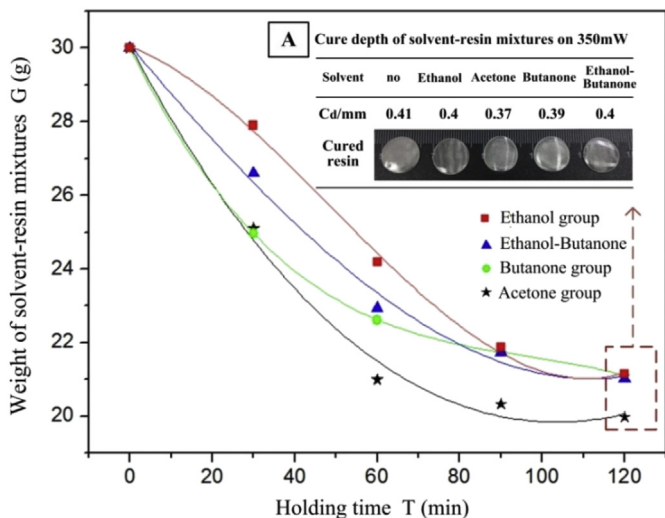


Fig. 4. The separation rate of solvent-resin mixtures and corresponding digital photographs of UV-cured samples after 2 h.

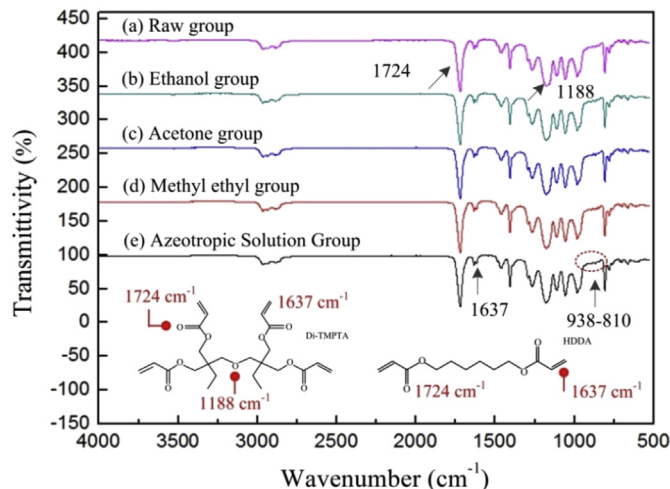


Fig. 5. FTIR spectra of different solvent-resin mixtures after separation at 70°C for 2 h.

peaks of out-of-plane C–H bending vibrations were found at 938, 847 and 810 cm^{-1} . As illustrated in Fig. 5, the peak, located at 1637, 938, 847 and 810 cm^{-1} , disappeared after ultraviolet irradiation, indicating the opening of C=C bonds in Di-TMPTA and HDDA and occurring of continuous polymerization. On the other hand, the FTIR spectra of the resins after separation (Fig. 5a–e) were found to be similar to the raw material. Hence, no chemical reaction occurred between the resin and solvent at 70 °C. Finally, based on compatibility and separation rate, the butanone/ethanol azeotropic solution was chosen as the solvent in subsequent experiments, which rendered a negligible effect on the polymerization of resins.

3.1.2. Dispersion of SiC whiskers in the ceramic paste

3D-printed $\text{SiC}_w/\text{Al}_2\text{O}_3$ green bodies, with different whisker contents, were degreased at 700 °C for 2 h, followed by SEM and EDS analysis. As shown in Fig. 6a–c, the gradual increase in SiC_w content did not lead to whisker agglomeration. Hence, the proposed method resulted in a uniform dispersion of SiC_w in the ceramic paste. The polar ethanol and butanone solvents eliminated the static charges from the surface of SiC_w and weakened the interactions between SiC whiskers [26]. The PEG-400 surfactant, with hydrophilic polyoxyethylene ($-\text{CH}_2\text{CH}_2\text{O}-$), significantly reduced the surface tension of the solvent and facilitated the wetting of solid surface [27]. Moreover, the hydrophilic oxygen atoms in the molecular chain of PEG-400 can also produce strong Van der Waals affinity to the hydroxyl groups ($-\text{OH}$) adsorbed on the SiC_w surface, forming a layer with a certain thickness on whiskers surface and preventing the agglomeration of SiC_w . Finally, in terms of the dispersion process, wet ball milling and stirring can provide enough kinetic energy for dispersion. Hence, SiC_w were uniformly dispersed in Al_2O_3 powder and corresponding paste. In addition, as illustrated in Fig. 6, the drawing ratio of whiskers was ~50 and the surface morphology remained intact, which show that ball milling and stirring did not damage SiC whiskers. The EDS analysis confirmed the presence of Al, O, Si and C, which indicates that oxidation and chemical reactions did not occur during degreasing process due to the presence of argon protection (Fig. 6c).

3.2. Effect of SiC_w content on performance of ceramic paste

3.2.1. Rheological properties

Fig. 7 (a) shows the relationship between shear rate and viscosity of $\text{SiC}_w/\text{Al}_2\text{O}_3$ paste with different amounts of SiC whiskers. The viscosity of $\text{SiC}_w/\text{Al}_2\text{O}_3$ paste decreased with increasing shear rate, which conforms to the non-Newtonian pseudoplastic fluid model [28]. When the shear rate was varied from 10 to 30 s^{-1} , the paste viscosity of 10 vol % SiC_w group rapidly decreased from 43,500 mPa s to 20,100 mPa s, featuring a shear-thinning effect. When the shear rate was increased from 60 to 100 s^{-1} , the viscosity continuously decreased to a lower level from 14,500 mPa s to 10,000 mPa s and attained a stable value, which is suitable for the paste coating process during SL 3D printing [29]. And when the layering thickness is 0.05 mm here, the shear rate value (10 s^{-1} , 30 s^{-1} , 60 s^{-1} , 100 s^{-1}) determine the corresponding speed of the blade (0.5 mm/s, 1.5 mm/s, 3 mm/s, 5 mm/s) in the coating process. The viscosity of $\text{SiC}_w/\text{Al}_2\text{O}_3$ paste was determined by the energy consumed due to the interaction of whiskers and particles, as well as the resistance of whiskers to liquid flow. The average grain size of Al_2O_3 particles was 1 μm , whereas the average diameter of SiC_w was ~0.5 μm , which can approximately result in strong interactions among the paste during flow. Therefore, the content and dimensions (diameter and aspect ratio) of SiC_w render obvious influence on the rheological behavior of the resulting paste. At low shear rates (0–30 s^{-1}), the viscosity of paste significantly increased with increasing SiC_w content. The viscosity of pure Al_2O_3 paste was 8500 mPa s at the shear rate of 30 s^{-1} , whereas the viscosity increased to 29,500 mPa s at SiC_w content of 15 vol %. During the paste coating, SiC_w whiskers and Al_2O_3 particles formed an unstable overlapping structure, which is sensitive to the shear rate [30]. When ceramic paste encounters shear stress, the cross structure is destroyed and directionally aligned. Also, the viscosity of each paste tends to converge to the same value after 100 s^{-1} . Therefore, Einstein formula [31] can be used to describe the relationship between relative viscosity (η_r) and the content of spherical particles (ϕ_p):

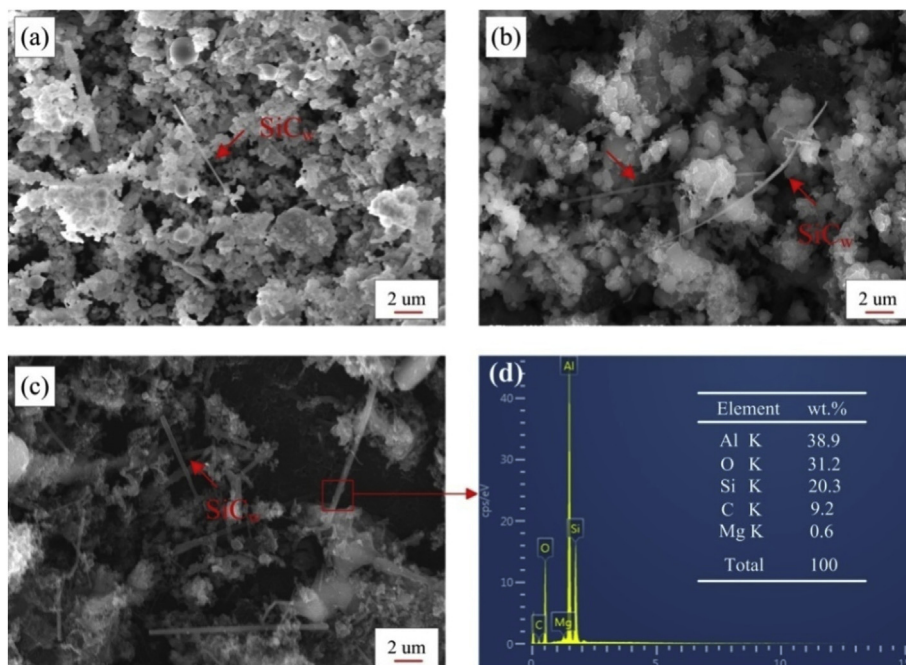


Fig. 6. SEM images of $\text{SiC}_w/\text{Al}_2\text{O}_3$ UV-cured paste with (a) 5 vol % SiC_w , (b) 10 vol % SiC_w and (c) 15 vol % SiC_w ; and (d) EDS analysis of composite Al_2O_3 paste with 15 vol % SiC_w .

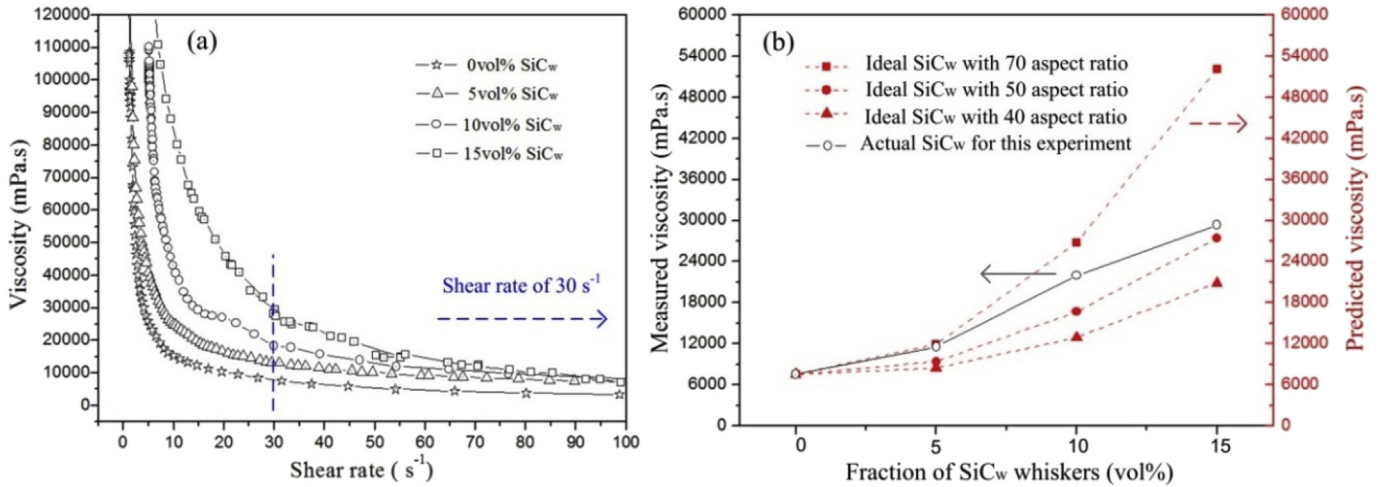


Fig. 7. The relationship between shear rate and viscosity of SiC_w/Al₂O₃ paste with different amounts of SiC whiskers. $\eta = \alpha \eta_0 \left[f_a (1 + 2.5\phi_p) + f_b \left(1 + \left(2.5 + \frac{\phi_w^2}{16} \right) \phi_w \right) \right]$

$$\eta_r = 1 + 2.5\phi_p \quad (1)$$

The relationship between η_r of SiC whiskers (aspect ratio: J) and whiskers content (ϕ_w) can be given as [32]:

$$\eta_r = 1 + \left(2.5 + \frac{J^2}{16} \right) \phi_w \quad (2)$$

Therefore, the viscosity of SiC_w/Al₂O₃ composite dispersion system can be given as:

$$\eta = \alpha \eta_0 \left[f_a (1 + 2.5\phi_p) + f_b \left(1 + \left(2.5 + \frac{J^2}{16} \right) \phi_w \right) \right] \quad (3)$$

where η refers to the apparent viscosity of SiC_w/Al₂O₃ paste; η_0 represents the viscosity of UV resin (248 mPa s); ϕ_p corresponds to the content of Al₂O₃ particles in the dispersion system; ϕ_w denotes the content of SiC whiskers; f_a and f_b correspond to volume percentage of particles and whiskers, respectively; and α denotes the correction factor (13.54), which can be achieved by using the number of experiments and numerical regression analysis. Herein, SiC whiskers, with an aspect ratio of ~50, were used to prepare the composite paste and its viscosity was measured at 30 s⁻¹ (Fig. 7b). One should note that the change in paste viscosity with different amounts of SiC whiskers remained consistent with the predicted values of Eq. (3), as shown in Fig. 7 (b). At the whiskers content of 10 vol %, the viscosity of SiC_w/Al₂O₃ paste is influenced by the aspect ratio of SiC whiskers. When the aspect ratio was increased from 40 to 70, the corresponding paste viscosity sharply increased from ~12,000 mPa s to ~27,000 mPa s, which can be ascribed to the overlapping and winding of longer SiC whiskers.

3.2.2. Curing properties

As shown in Fig. 8a-b, the curable ceramic pastes were solidified into single lines by ultraviolet laser irradiation (spot diameter: 40 μm) during SL 3D printing. Also, several lines overlapped to form a cured layer. Finally, a certain complex structure was superimposed layer-by-layer. During this process, a single line can be considered as a basic component unit, and its shape and size (curing depth C_d , line width L_w) determine the accuracy of the 3D-printed parts. Owing to the light scattering effect of ceramic

particles, the curing depth of photosensitive paste is smaller than the pure resin. On the other hand, the width of photosensitive paste is larger than the pure resin. Hence, the curing characteristics of single lines of SiC_w/Al₂O₃ paste should be investigated to determine 3D printing parameters, such as layer depth (L_d) and laser scanning distance (H_s). The Beer-Lambert formula [33] can be used to express the relationship between C_d and penetration depths (D_p):

$$C_d = D_p \ln \frac{E}{E_c} \quad (4)$$

where E_c refers to the critical exposure of paste and E represents the laser exposure on paste surface [34,35]:

$$E = \frac{\sqrt{2}P}{\sqrt{\pi}w_0v} \quad (5)$$

where P corresponds to ultraviolet laser power; w_0 denotes the laser spot radius; and v refers to the laser scanning speed.

The honeycomb structure was reduced in size until the internal grid structure was only composed of single scanning lines. The single lines were fabricated by using different laser powers (P). Then, the LSM microscope was used to measure L_w and C_d , as shown in Fig. 8c, d. Finally, L_w and C_d of single lines of ceramic pastes, containing different amounts of SiC_w whiskers, were counted under different UV laser exposures (Fig. 9).

When laser power was increased from 102 mW to 425 mW, the E value increased from 25.43 mJ/cm² to 105.97 mJ/cm², whereas C_d of SiC_w/Al₂O₃ pastes, with 5, 10 and 15 vol % SiC whiskers, increased from 0.074 to 0.098 mm, 0.068–0.085 mm, and 0.061–0.074 mm, respectively. However, compared with pure Al₂O₃ paste, the growth rate of C_d has been reduced. Moreover, under the same laser power, C_d significantly decreased with increasing SiC_w content. Based on Fig. 9, paste penetration depth (D_p) and critical exposure (E_c) are calculated and summarized in Table 1.

The increase in SiC_w content resulted in a sharp increase in E_c of the paste, leading to the intensification of light scattering and hindering the curing of ceramic paste. Under the same concentration of SiC_w and Al₂O₃ solutions (0.0026 wt%), the transmissivity of SiC_w (18.88%) is far lower than Al₂O₃, as shown in Fig. 10. The refractive index of SiC_w is higher than Al₂O₃. Hence, at the same solution concentration, the percentage absorptivity (ϵ , 101.67) of

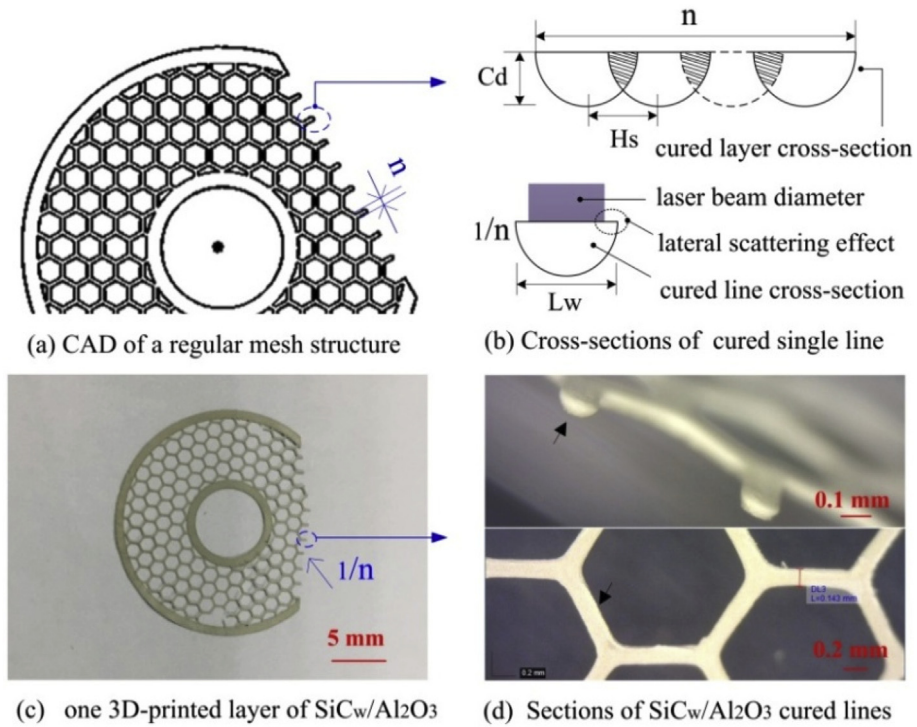


Fig. 8. The fabrication process of basic building units via SL 3D printing technology.

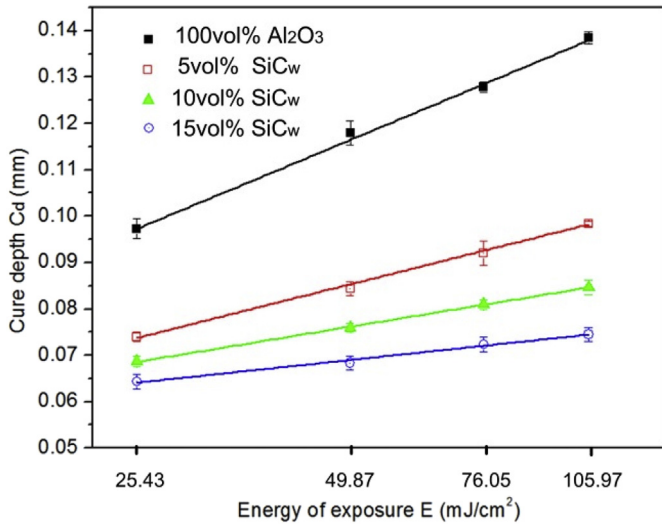


Fig. 9. The curing depth of UV-curable ceramic pastes with different amounts of SiC_w whiskers.

Table 1
Photosensitive parameters of SiC_w/Al₂O₃ pastes with different amounts of SiC_w whiskers.

Parameter	Pure Al ₂ O ₃	5 vol% SiC _w	10 vol% SiC _w	15 vol% SiC _w
D _p /μm	31.1	17.24	11.31	7.3
E _c /mJ/cm ²	2.18	4.63	12.42	20.05

SiC_w under the incident ultraviolet light (355 nm) is much higher than Al₂O₃ particles (75.61).

Owing to the strong scattering effect of SiC_w under the influence of ultraviolet light (355 nm), it is necessary to further investigate

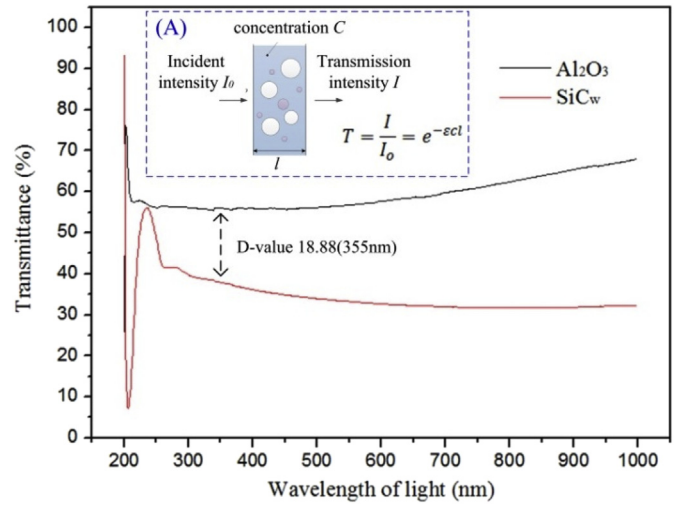


Fig. 10. UV-Vis spectra of Al₂O₃ and SiC_w dispersions in ethanol solvent.

the effect of SiC_w content on curing depth of photosensitive paste. The photosensitive parameters of ceramic pastes, with different amounts of SiC_w whiskers, are shown in Fig. 11. The empirical relationship between SiC_w content (φ) and D_p and E_c can be given as:

$$D_p = 31.05 \cdot (40720)^{-\varphi_{SiCw}} \quad (6)$$

$$E_c = 2.48 \cdot (3.05)^{\varphi_{SiCw}} \quad (7)$$

Thus, the relationship between curing depth (C_d), SiC_w content, laser power and scanning speed (v) can be given as:

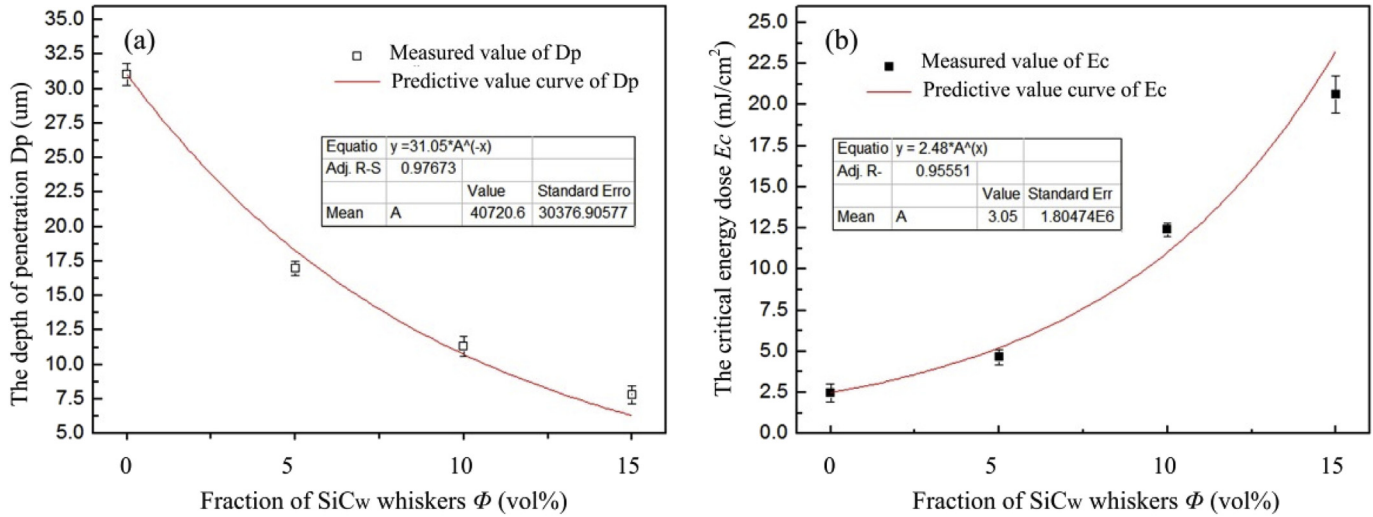


Fig. 11. Influence of SiC whiskers content on photosensitive parameters, i.e., D_p and E_c , of SiC_w/Al₂O₃ paste.

$$C_d(\varnothing_{SiCw}) = 31.05 \cdot 40720^{-\varnothing_{SiCw}} \cdot 10^{-3} \left[5.11 + \ln\left(\frac{P}{v} \cdot 3.05^{-\varnothing_{SiCw}}\right) \right] \times C_d(\varnothing_{Si3N4}) = 0.0639 \cdot 5.5^{-\varnothing_{Si3N4}} \left[6.519 + \ln\left(\frac{P}{v} \cdot 11.2^{-\varnothing_{Si3N4}}\right) \right] \times \quad (8)$$

There is a linear relationship between the depth and width of curing line. Also, the line width (L_w) can be indirectly obtained by analyzing C_d value from Fig. 12:

$$L_{w(0vol\%)} = 2.485C_d - 0.065 \quad (9)$$

$$L_{w(5vol\%SiCw)} = 3.283C_d - 0.101 \quad (10)$$

$$L_{w(10vol\%SiCw)} = 3.552C_d - 0.096 \quad (11)$$

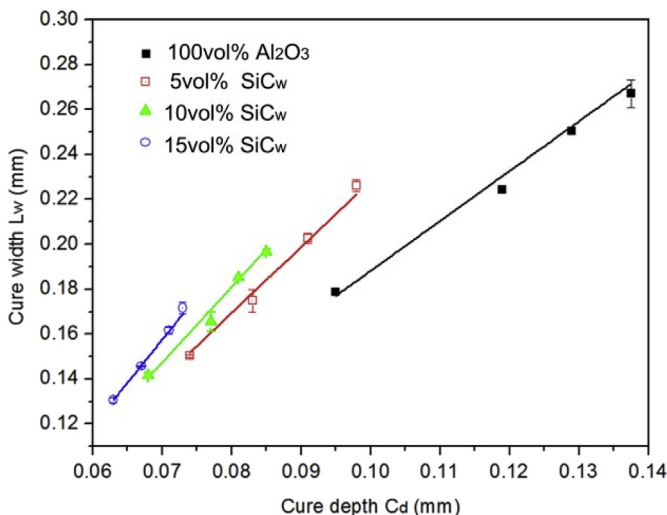


Fig. 12. The cured line width (L_w) as a function of curing depth (C_d).

$$L_{w(15vol\%SiCw)} = 4.149C_d - 0.137 \quad (12)$$

It has been reported that layer thickness L_d should be lower than single line curing depth C_d during the SL 3D printing process. And the scanning distance (H_s) should be optimized between zero and the single line width value (L_w), to obtain effective connection between adjacent single curing lines. Therefore, Eqs. 6–12 can be used to design and optimize the 3D printing parameters (L_d , H_s) of Al₂O₃ paste with different amounts of SiC_w (5–15 vol %).

3.3. Characterization and microstructure of SL 3D-printed SiC_w/Al₂O₃ ceramics components

3.3.1. Mechanical properties

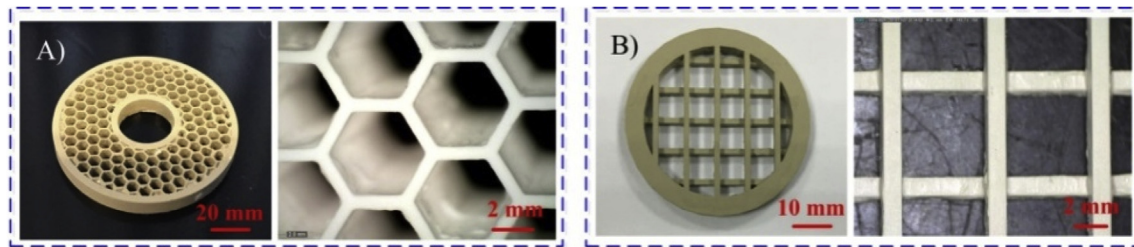
As given in Table 2, the maximum flexural strength, fracture toughness, hardness and relative density of as-fabricated SiC_w/Al₂O₃ ceramic were 405 ± 98 MPa, 7.1 ± 1.20 MPa m^{1/2}, 17.6 ± 0.78 GPa and ~99%, respectively. Compared with pure Al₂O₃ ceramic, SiC_w-toughened Al₂O₃ ceramics (5–15 vol %) exhibited superior fracture toughness, corresponding to an increase of 31% after the incorporation of SiC whiskers. Moreover, the flexural strength increased with increasing whiskers' content, rendering the maximum value of 405 MPa at SiC_w content of 10 vol %. However, the excessive amount of whiskers (15 vol %) resulted in lower flexural strength of SiC_w/Al₂O₃ ceramics. Also, the relative density of composite ceramics decreased from 99.4% to 93.2% when the SiC_w content was increased from 10 to 15 vol %. It can be concluded that a lower relative density leads to a lower flexural strength of SiC_w/Al₂O₃ ceramics. And an optimal amount of SiC_w toughening phase (5–10 vol %) is required to obtain desired mechanical properties. However, the excessive whiskers' content hinders the densification during sintering and leads to inferior relative density, flexural strength and hardness.

3.3.2. Microstructure

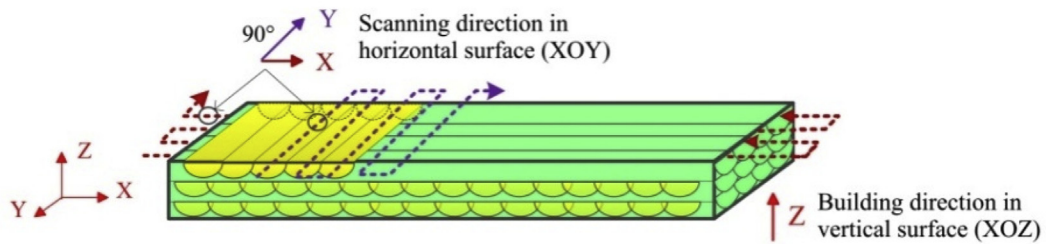
Fig. 13 (a, b) present the influence of x/y -raster scanning paths and layer-by-layer manufacturing characteristics of SL 3D printing on surface roughness of as-prepared SiC_w/Al₂O₃ ceramic components. Owing to the typical laser scanning paths, the horizontal and vertical surfaces (XOY and XOZ) of the SiC_w/Al₂O₃ ceramic exhibited different surface roughness values. One should note that the traces of scanning paths were not observed in the XOY surface. Also, the

Table 2
Mechanical properties of SL 3D-printed and sintered SiC_w/Al₂O₃ ceramics.

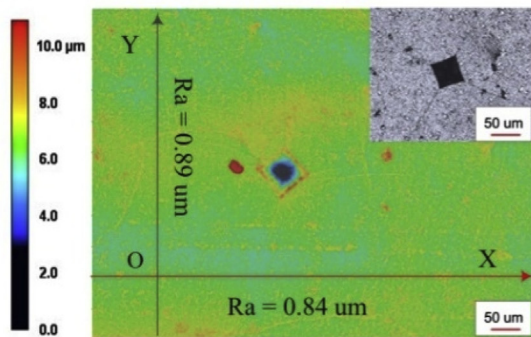
Parameter	0 vol %SiC _w	5 vol%SiC _w	10 vol %SiC _w	15 vol %SiC _w
Flexural strength/MPa	389 ± 71	394 ± 75	405 ± 98	355 ± 108
Fracture toughness/MPa·m ^{1/2}	5.5 ± 0.95	6.60 ± 1.03	7.1 ± 1.20	6.8 ± 1.37
Vickers hardness/GPa	18.0 ± 0.80	17.6 ± 0.78	17.6 ± 0.84	17.3 ± 0.94
Relative density/%	99.4 ± 0.2	99 ± 0.3	97.1 ± 0.2	93.2 ± 0.5



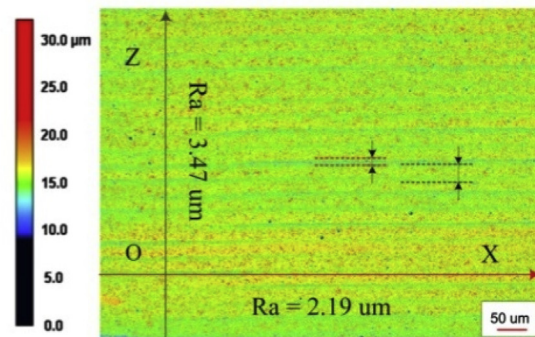
(a) 3D-printed and sintered complex structural SiC_w/Al₂O₃ parts and their detail morphologies



(b) Schematic representing the x/y-raster scanning path of SL process



(c) LSM morphology of XOY surface after 3D-printing and sintering



(d) LSM morphology of XOZ surface after 3D-printing and sintering

Fig. 13. LSM morphology represents the surface roughness in different directions on horizontal and vertical surfaces of as-prepared SiC_w/Al₂O₃ ceramics.

surface roughness in both directions (OX/OY) exhibited a negligible variation (0.84–0.89 μm), as shown in Fig. 13c. Hence, the XOY printed surface of as-prepared ceramic demonstrated nearly isotropic characteristics. However, layer-by-layer morphology has been observed in Fig. 13d, which increased the R_a of XOZ surface. The highest R_a (3.47 μm) was achieved in the OZ direction, which corresponds to the building direction of 3D printing. Moreover, the R_a value of 2.19 μm was observed in the OX direction on XOZ surface. Hence, XOZ rendered anisotropic surface roughness, which is different from the XOY surface.

As shown in Fig. 14a and b, some of the SiC_w whiskers are uniformly embedded in the grain boundaries of Al₂O₃ grains, indicating the uniform distribution of SiC whiskers in alumina matrix

after SL 3D printing and sintering. Furthermore, the average diameter of Al₂O₃ grains was approximately 2 μm and some apparent grain growth (5 μm) has been observed after sintering. Moreover, some mini pores, with a special oval feature, remained due to rapid sintering and the addition of SiC_w whiskers. Furthermore, the fracture morphology of SiC_w/Al₂O₃ ceramics is presented in Fig. 14c and d, showing that 10 vol % SiC_w/Al₂O₃ composite exhibits a mixed-mode of intergranular and transgranular fracture. One should note that the transgranular fracture easily occurs around the position of larger grains (>3 μm) because large grains cannot withstand large shear stress. Also, the interaction force between grains is higher than the internal strength of grains, resulting in a transgranular fracture. In addition, a number of

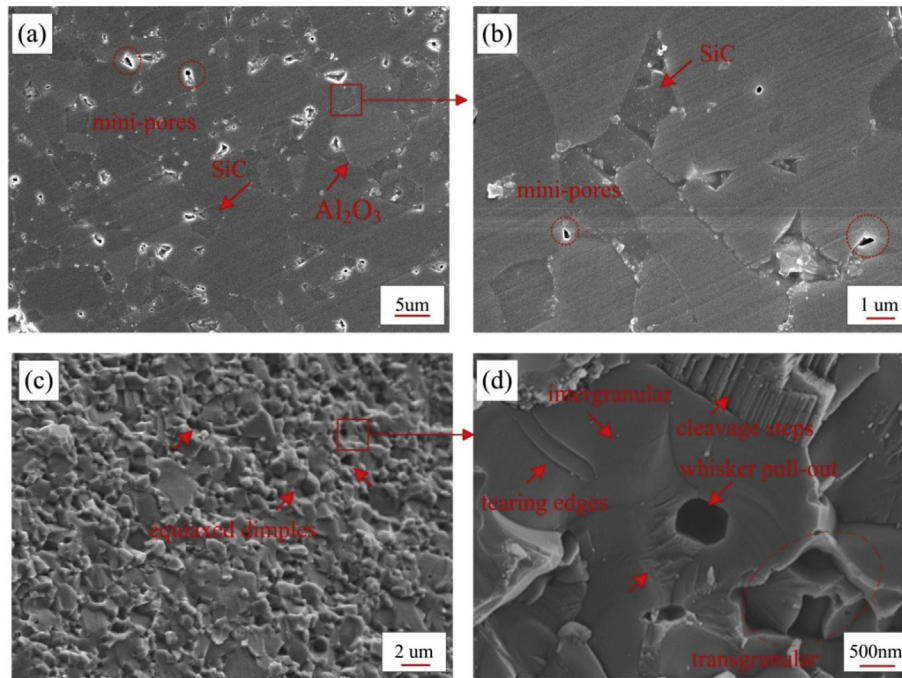


Fig. 14. SEM images of (a, b) polished and (c, d) fracture surfaces of sintered 10 vol % $\text{SiC}_w/\text{Al}_2\text{O}_3$ composite ceramic.

equiaxed dimples and pitting dimples were observed in the fractured surfaces. Moreover, regular-shaped deep holes, with a diameter of ~ 500 nm, were found at the fracture surface, indicating the improvement in fracture toughness of SiC_w -containing composites due to the whisker pull-out mechanism [36]. During crack propagation, the whisker is pulled-out from the matrix when a crack encounters a high strength SiC_w whisker. At the same time, the friction between SiC_w whisker and matrix consumes the energy of external loading, resulting in superior toughness of $\text{SiC}_w/\text{Al}_2\text{O}_3$ composite ceramic. Therefore, river-like patterns (cleavage steps) and tearing edges have been observed on the fracture surface around the whisker pull-out hole. The nano-step pattern size of Al_2O_3 during fracture is $\sim 5\text{--}50$ nm, whereas the lattice parameter (a) of tripartite lattice structure is 5.14 Å. Hence, the fracture process of $\alpha\text{-Al}_2\text{O}_3$ around the whisker is composed of about $10\text{--}100$ cells. It can be concluded that the cleavage fracture mode and dimple fracture mode occurred around SiC_w whisker. When the whisker is pulled-out from the matrix, the microcracks around the matrix absorb more energy, leading to the improved fracture toughness of composite ceramics.

Furthermore, the fracture morphology of $\text{SiC}_w/\text{Al}_2\text{O}_3$ ceramics with 5 vol % and 15 vol % whiskers was also presented in Fig. 15a and b. Compared with the 10 vol % $\text{SiC}_w/\text{Al}_2\text{O}_3$ composite ceramic,

the 5 vol % $\text{SiC}_w/\text{Al}_2\text{O}_3$ sample exhibited a similar mixed-mode of intergranular and transgranular fracture. A number of equiaxed dimples and pitting dimples were also observed in the fractured surfaces. And a deep pore was observed on the fracture surface due to the pulling-out of whisker, indicating a notable toughening mechanism of whisker pulling out. In contrast, more unflat fracture surface emerged for the 15 vol % $\text{SiC}_w/\text{Al}_2\text{O}_3$ material in Fig. 15b, which proved that the intergranular fracture mode was dominant. But some abnormal deep cavities ($2\ \mu\text{m}$ in diameter) were left on the fracture surface. There cavities were distinguishable from whiskers pulling-out pores because the whisker with a smaller size was also observed at the edge of the hole, as shown in Fig. 15b. Those large cavities distributing randomly in the composite ceramic would be negative to the mechanical properties of 15 vol % $\text{SiC}_w/\text{Al}_2\text{O}_3$ material.

4. Conclusions

(1) A butanone-ethanol azeotropic solvent was selected to facilitate the mixing and dispersion of particles, whiskers and photosensitive organic compounds. Then, 50 vol % solid content $\text{SiC}_w/\text{Al}_2\text{O}_3$ pastes, with SiC_w whiskers content of 5–15 vol %, were prepared by using ball milling, stirring and distillation. The solvent

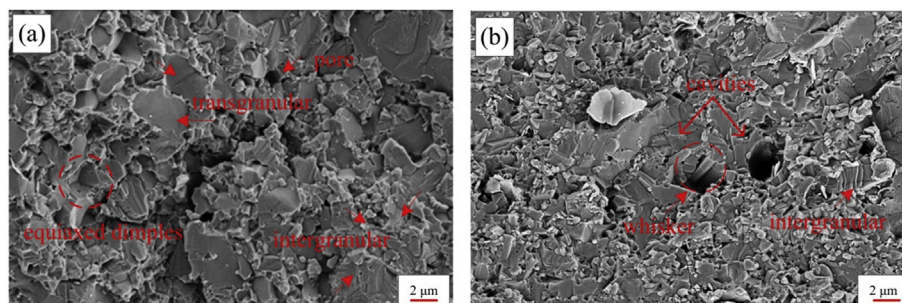


Fig. 15. SEM images of fracture surfaces of sintered $\text{SiC}_w/\text{Al}_2\text{O}_3$ composite ceramic: (a) 5 vol % SiC_w , (b) 15 vol %.

was separated in vacuum at 70 °C for about 2 h without weakening the polymerization of photosensitive resins. Simultaneously, SiC_w/Al₂O₃ ceramic pastes facilitated the dispersion and avoided the agglomeration of SiC whiskers.

(2) The rheological and curing properties of SiC_w/Al₂O₃ ceramic pastes were influenced by SiC_w content and dimensional parameters of SiC whiskers. Herein, an empirical equation was established to evaluate the relationship between SiC_w content, aspect ratio and viscosity of the ceramic paste. The 15 vol % SiC_w/Al₂O₃ composite, which SiC aspect ratio of ~50, consumed higher energy and rendered higher resistance to the liquid flow, resulting in the highest viscosity of 29,500 mPa s at the shear rate of 30 s⁻¹. Moreover, a modified equation was established to predicate the curing depth of ceramic pastes, with different amounts of SiC_w, in different 3D printing parameters, i.e., laser power and laser scanning speed. The 15 vol % SiC_w/Al₂O₃ composite ceramic exhibited superior light scattering properties, resulting in the lowest C_d of ~0.061 mm at the laser power of 102 mW and laser scanning speed of 8000 mm/s.

(3) Finally, complex-shaped SiC_w/Al₂O₃ ceramic components were prepared by using SL 3D printing technology, followed by debinding and sintering processes. The as-fabricated SiC_w/Al₂O₃ composite ceramic exhibited highest flexural strength, fracture toughness, hardness and relative density of 405 ± 98 MPa, 7.1 ± 1.20 MPa m^{1/2}, 17.6 ± 0.78 GPa and ≈99%, respectively. Furthermore, traces of scanning paths were not observed on the horizontal surface and R_a values exhibited negligible change (0.84–0.89 μm). However, the layer-by-layer morphology was observed in the vertical surface, which increased the R_a of building direction to 3.47 μm. Finally, SiC_w/Al₂O₃ composite ceramics exhibited mixed intergranular and transgranular modes of fracture, where the fracture toughness was improved by whisker pull-out and crack deflection mechanisms.

Declaration of competing interests

The authors declare that they have no known competing financial interests or personal relationships that could have appeared to influence the work reported in this paper.

CRedit authorship contribution statement

Hongyu Xing: Methodology, Formal analysis, Writing - original draft. **Bin Zou:** Conceptualization, Writing - review & editing. **Xinfeng Wang:** Formal analysis, Software. **Yifan Hu:** Data curation. **Chuanzhen Huang:** Conceptualization. **Kai Xue:** Investigation.

Acknowledgements

This project was National Natural Science Foundation of China (No. 51875319), and Key Research and Development Program of Shandong Province (2019GGX104049).

References

- [1] S. Yan, Y. Huang, D. Zhao, F. Niu, G. Ma, D. Wu, 3D printing of nano-scale Al₂O₃-ZrO₂ eutectic ceramic: principle analysis and process optimization of pores, *Addit. Manuf.* 28 (2019) 120–126.
- [2] Y. Zhang, A. Bandyopadhyay, Direct fabrication of compositionally graded Ti-Al₂O₃ multi-material structures using Laser Engineered Net Shaping, *Addit. Manuf.* 21 (2018) 104–111.
- [3] M. Gromada, A. Świeca, M. Kostecki, A. Olszyna, A. Cygan, Ceramic cores for turbine blades via injection moulding, *J. Mater. Process. Technol.* 220 (2015) 107–112.
- [4] J. Huang, Q. Liao, W. Fu, et al., Synthesis of Fe-doped alumina transparent ceramics by co-precipitation and vacuum sintering, *Ceram. Int.* 44 (2017). S0272884217321910.
- [5] X. Liu, H. Liu, C.Z. Huang, et al., High temperature mechanical properties of Al₂O₃ -based ceramic tool material toughened by SiC whiskers and nanoparticles, *Ceram. Int.* 43 (2016) 1160–1165.
- [6] Y.S. Wang, B. Zou, J.C. Wang, Y. Wu, C.Z. Huang, Effect of the progressive tool wear on surface topography and chip formation in micro-milling of Ti-6Al-4V using Ti(C₇N₃)-based cermet micro-mill, *Tribol. Int.* 141 (2020) 105–111.
- [7] B. Zhao, H. Liu, C.Z. Huang, et al., Fabrication and mechanical properties of Al₂O₃-SiC_w-TiC_{np} ceramic tool material, *Ceram. Int.* 43 (2017) 10224–10230.
- [8] A.N. Chen, M. Li, J. Xu, et al., High-porosity mullite ceramic foams prepared by selective laser sintering using fly ash hollow spheres as raw materials, *J. Eur. Ceram. Soc.* 38 (2018) 4553–4559.
- [9] S. Rangarajan, Q. Gang, N. Venkataraman, et al., Powder processing, rheology, and mechanical properties of feedstock for fused deposition of Si₃N₄ ceramics, *J. Am. Ceram. Soc.* 83 (2010) 1663–1669.
- [10] X. Du, S. Fu, Y. Zhu, 3D printing of ceramic-based scaffolds for bone tissue engineering: an overview, *J. Mater. Chem. B.* 6 (2018) 4397–4412.
- [11] X. Peng, Y. Jian, S. Shen, et al., Perovskite and organic solar cells fabricated by inkjet printing: progress and prospects, *Adv. Funct. Mater.* 27 (2017) 1703704–1703731.
- [12] Q.H. Chen, B. Zou, Q.G. Lai, Y. Wang, R.Q. Xue, H.Y. Xing, X. Fu, C.Z. Huang, P. Yao, A study on biosafety of HAP ceramic prepared by SLA-3D printing technology directly, *J. Mech. Behav. Biomed.* 98 (2019) 327–335.
- [13] X.Y. Liu, B. Zou, H. Xing, C.Z. Huang, The preparation of ZrO₂-Al₂O₃ composite ceramic by SLA-3D printing and sintering processing, *Ceram. Int.* (2019), <https://doi.org/10.1016/j.ceramint.2019.09.054>.
- [14] C. Griffin, J. Daufenbach, S. Mcmillin, Desk-top manufacturing: LOM vs pressing, *Am. Ceram. Soc. Bull.* 73 (1994) 109–113.
- [15] A. Bandyopadhyay, K. Das, Application of fused deposition in controlled microstructure metal-ceramic composites, *Rapid Prototyp. J.* 12 (2006) 121–128.
- [16] K. Shahzad, J. Deckers, J.P. Kruth, et al., Additive manufacturing of alumina parts by indirect selective laser sintering and post processing, *J. Mater. Process. Technol.* 213 (2013) 1484–1494.
- [17] J. Yoo, M.J. Cima, S. Khanuja, et al., Structure ceramic components by 3D printing, *Solid Freeform Fabr. Proc.* 94 (1993) 40–50.
- [18] C.M. Larson, J.J. Choi, P.A. Gallardo, et al., Direct ink writing of silicon carbide for microwave optics, *Adv. Eng. Mater.* 11 (2015) 1–7.
- [19] M.L. Griffith, J.W. Halloran, Freeform fabrication of ceramics via stereolithography, *J. Am. Ceram. Soc.* 79 (2010) 2601–2608.
- [20] Z.C. Eckel, C. Zhou, J.H. Martin, et al., Additive manufacturing of polymer-derived ceramics, *Science* 351 (2016) 58–62.
- [21] E. Zanchetta, M. Cattaldo, G. Franchin, et al., Stereolithography of SiOC ceramic microcomponents, *Adv. Mater.* 28 (2016) 370–376.
- [22] H.Y. Xing, B. Zou, Q.G. Lai, et al., Preparation and characterization of UV curable Al₂O₃ suspensions applying for stereolithography 3D printing ceramic microcomponent, *Powder Technol.* 338 (2018) 153–161.
- [23] X.S. Fu, B. Zou, H. Xing, L. Li, et al., Effect of printing strategies on forming accuracy and mechanical properties of ZrO₂ parts fabricated by SLA technology, *Ceram. Int.* 45 (2019) 17630–17637.
- [24] B. Liu, C.Z. Huang, M. Gu, et al., Preparation and mechanical properties of in situ growth TiC whiskers toughening Al₂O₃ ceramic matrix composite, *Mat. Sci. Eng. A.* 460 (2007) 146–148.
- [25] S. Suárez, E. Ramos-Moore, B. Lechthaler, et al., Grain growth analysis of multiwalled carbon nanotube-reinforced bulk Ni composites, *Carbon* 70 (2014) 173–178.
- [26] A. Catellani, G. Cicero, G. Galli, Wetting behavior of low-index cubic SiC surfaces, *J. Chem. Phys.* 124 (2006), 024707, <https://doi.org/10.1063/1.2140690>.
- [27] M. Akermi, N. Sakly, R.B. Chaabane, et al., Effect of PEG-400 on the morphology and electrical properties of ZnO nanoparticles application for gas sensor, *Mater. Sci. Semicond. Process.* 16 (2013) 807–817.
- [28] E. Mitsoulis Fountain, Flow of pseudoplastic and viscoplastic fluids, *J. Non-Newton Fluid.* 165 (2010) 45–55.
- [29] M. Jabbari, J. Spangenberg, J.H. Hattel, Particle migration using local variation of the viscosity (LVOV) model in flow of a non-Newtonian fluid for ceramic tape casting, *Chem. Eng. Res. Des.* 109 (2016) 226–233.
- [30] A.M. Bercea, N. Patrick, Shear dynamics of aqueous suspensions of cellulose whiskers, *Macromolecules* 33 (2000) 6011–6016.
- [31] A.J. Hughes, The Einstein relation between relative viscosity and volume concentration of suspensions of spheres, *Nature* 173 (1954), 1090–1090.
- [32] L. Bergström, Rheological properties of Al₂O₃-SiC whisker composite suspension, *J. Mater. Sci.* 3 (1996) 5257–5270.
- [33] S.P. Gentry, J.W. Halloran, Light scattering in absorbing ceramic suspensions: effect on the width and depth of photopolymerized features, *J. Eur. Ceram. Soc.* 35 (2015) 1895–1904.
- [34] F.A. Rueggeberg, W.F. Caughman, C.J. Jr., Effect of light intensity and exposure duration on cure of resin composite, *Operat. Dent.* 19 (1994) 26–32, [https://doi.org/10.1016/0022-3913\(94\)90255-0](https://doi.org/10.1016/0022-3913(94)90255-0).
- [35] J.H. Lu, J.P. Youngblood, Adhesive bonding of carbon fiber reinforced composite using UV-curing epoxy resin, *Compos. B Eng.* 82 (2015) 221–225.
- [36] C.M. li, M. Xing, Y. Hong, L. Li, Influence of high temperature on strength, ultrasonic velocity and mass loss of calcium carbonate whisker reinforced cement paste, *Compos. B Eng.* 163 (2019) 438–446.